# $LnCrTeO_6$ (Ln= La, Pr, Nd) octahedral distortions and optical characterization

By

Katheryn R. Cruz

Presented to the Faculty of the Graduate School of

The University of Texas at Arlington in Partial Fulfillment

of the requirements

for the Degree of

Master of Science in Chemistry and Biochemistry

THE UNIVERSITY OF TEXAS AT ARLINGTON

August 2022

Supervising Committee:

Robin Macaluso, Supervising Professor

Frank Foss

Sherri McFarland

## Abstract

$LnCrTeO_6$ (Ln= La, Pr, Nd) octahedral distortions and optical characterization

Katheryn R. Cruz, Master of Science

University of Texas at Arlington, 2022

Supervising professor: Robin Macaluso

$LnCrTeO_6$ (La, Pr, Nd) were synthesized to analyze the local coordination environments of $Ln^{3+}$, $Cr^{3+}$, and $Te^{6+}$ cations. Structural characterization was performed using X-ray diffraction (XRD) and optical properties were examined using diffuse reflectance spectroscopy (DRS). DRS data was further processed using the Kubelka-Munk function and a Tauc plot was generated to determine the direct and indirect band gap of these semiconducting materials. The superstructure peak corresponding to the (101) plane displayed relatively weak intensities in all samples and decreased in intensity from La to Nd. The (002) and (100) peak intensities varied across the samples. All cation octahedra displayed distorted bond lengths and angles. In each sample, the Cr–O bond lengths were atypical of Cr (III) bond lengths; values were closer to Cr(IV)–O bond distances, suggesting, the possible presence of Cr(IV) in $LnCrTeO_6$ (La, Pr, Nd).

Table of Contents

## Literature Review

### The $PbSb_2O_6$ Structure Type

Magnéll first discovered the $PbSb_2O_6$ structure type, which can be described with the *P*3*m*1 space group and unit cell dimensions of $a \approx 5.298$ Å and $c \approx 5.372$ Å.[1,2] The crystal structure is comprised of layers of edge-sharing $SbO_6$ octahedra stacked along the *c*-axis. The $Pb^{2+}$ cations are located between layers of $SbO_6$ octahedra (Fig. 1).[2-8]

Many compounds with the $PbSb_2O_6$ structure type possess unique characteristics and have shown potential application in a wide range of fields, such as thermoelectrics, oxidation reactions, and fluorescents.[9-11] For example, a series of $LnFe_{0.5}Sb_{1.5}O_6$ (Ln= La- Sm) compounds, were found to be suitable catalysts in CO oxidation reactions. Rare earth atoms located in voids between layers, depending on the rare earth, the interlayer space can be adjusted, in this case larger rare earths were favorable. Samples showed excellent thermal stability and suggested that their layered nature could be favorable when acting as a catalyst.[9] $BiGeSbO_6$, exhibited potential as a phosphor due to its unique luminescent properties which was suggested to be due to the structural features differing from other $Bi^{3+}$ doped compounds.[10] The two-dimensional structure of $PbSb_2O_6$-type materials provides electron pathways which help to decrease the lattice thermal conductivity, and increase electrical conductivity in $BaBi_2O_6$, making it suitable for thermoelectric applications. Furthermore, doping with La tunes the Fermi level energy into the conduction band and suppresses thermal conductivity (because of the mass difference between La and Ba). [11]

The $PbSb_2O_6$ structure type can be adopted by multiple classes of compounds including antimonates, arsenates, ruthenates, and tellurates, resulting in numerous structural modifications.[12] For example, in $A(II)GeTeO_6$ (A= Mn, Cd, Pb) tellurates, deviation from the

$PbSb_2O_6$ parent structure, caused by cation ordering, leads to a reduction in symmetry to the non-centrosymmetric *P*312 space group. The $Ge^{+4}$ and $Te^{+6}$ cations form ordered octahedral layers and the authors suggest this ordering could be due to the Coulombic repulsion between $Ge^{+4}$ and $Te^{+6}$ cations. It was found that the size of the A cation should be at least 0.8 Å to stabilize the modified PbSb2O6 structure.[13] In 2016, Kim et al. synthesized BiM(III)$TeO_6$ (M= Cr, Mn, Fe) compounds and examined crystal structures, cation ordering, and magnetic properties. The degree of ordering is dependent upon the choice of M; the Cr/Te ratio of 80:20 is less ordered than the Fe and Mn analogs. While $BiCrTeO_6$ and $BiFeTeO_6$ crystal structures belong to the $P\bar{3}$ space group, the complete ordering between $MnO_6$ and $TeO_6$ octahedra result in a more complex, lower symmetry structure with the monoclinic $P2_1/c$ space group. The lower symmetry of $BiMnTeO_6$ is attributed to Jahn-Teller distortions of $MnO_6$ octahedra.

The B-site disorder affects the magnetic ordering of $M^{3+}$ (M = Cr, Fe) because of the difference in concentrations of magnetic nearest and next nearest neighbor interactions. $BiCrTeO_6$ exhibited a broad Neel temperature, $T_N$ ~17 K, indicating antiferromagnetic ordering. A sharper antiferromagnetic transition was seen with $BiFeTeO_6$ and $BiMnTeO_6$ with $T_N$ of ~ 11 K and ~ 9.5 K respectively, suggesting long-range order between magnetic cations.[14]

a) b)

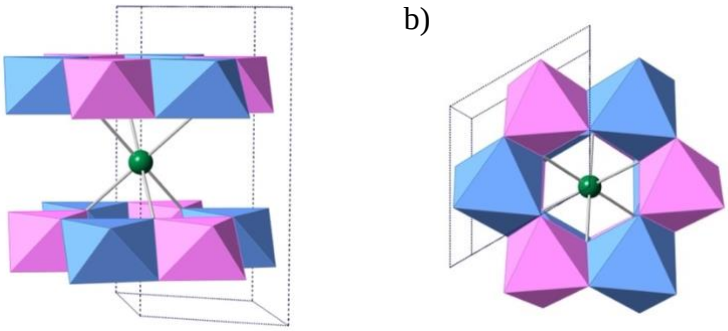

Figure 1: Crystal structure of $LnCrTeO_6$ (Ln= La, Pr, Nd) with layers of ordered $CrO_6$ (pink shading), $TeO_6$ (blue shading) octahedra, and Ln shown in green along the a) *c*-axis and b) *ab*-plane.

## $LnCrTeO_6$ (Ln= lanthanide)

In 1969, $LnCrTeO_6$ (Ln = La, Pr, Nd, Sm, Ed, Gd, Tb, Dy, Ho, Er, Tm, Yb, Y) were first reported to adopt a modified $PbSb_2O_6$ structure type. The structure of $LnCrTeO_6$ can be viewed as cationic substitutions of $La^{3+}$ for $Pb^{2+}$ and $Te^{6+}$ and $Cr^{3+}$ for $Sb^{5+}$, creating layers of edge-sharing $TeO_6$ and $CrO_6$ octahedra with each layer separated by $LnO_6$ octahedra (Figure 1).[4, 6, 7] $LaCrTeO_6$ has been investigated as a potentially blue and/or green pigment with excellent thermal stability and color saturation, therefore, making it a promising pigment for ceramics applications (Gayo, 2014). In previous structural studies of $LnCrTeO_6$ compounds, an additional weak-intensity (101) peak in X-ray diffraction (XRD) data has been observed and attributed to a superstructure.[3,4,6] Superstructure results from additional ordering of two or more atoms – in this case, $Cr^{3+}$ and $Te^{4+}$ – and results in a doubling of the *c*-axis and modification of the space group from $P3m1$ to $P\bar{3}$.

Although the signature (101) peak describing the superstructure of $LnCrTeO_6$ (Ln = La, Pr, Nd, Sm, Ed, Gd, Tb, Dy, Ho, Er, Tm, Yb, Y) has been described in several papers, [3-7] many questions regarding structural disorder and distortions remain unanswered. Kasper et al. observed a decrease in the relative intensity of the (101) superstructure peak with decreasing ionic radii of the lanthanide. The trend in superstructure peak intensity has been correlated to the decrease of the unit cell volume (lanthanide contraction) and a change in hue from blue-green to blue-gray (with decreasing unit cell volume).[3] However, careful qualitative analyses of these superstructure peaks

have yet to be performed. Furthermore, variation in colors suggests the possibility of strong crystal-field splitting of $Cr^{3+}$ -octahedra[3,6]; the structural distortions have yet to be characterized.

It was also found that for $LnCrTeO_6$ (Ln= La, Pr, Nd, Sm, Ed, Gd, Tb, Dy, Ho, Er, Tm, Yb, Y) that the experimental relative peak intensities of the (101) superstructure reflection were significantly lower than the calculated (101) peak intensity, with the peak only about 5% compared to the most intense peak in the pattern.[7] Because of the difference between the intensity of the (101) superstructure peak in the experimental and calculated XRD patterns, it has been suggested that there is some degree of disorder between $Cr^{3+}$ and $Te^{4+}$.[3,8] However, the nature of this disorder remains to be characterized.

The goals of this thesis are to synthesize $LnCrTeO_6$ (Ln= La, Pr, Nd) using solid-state techniques, determine their crystal structures and measure their optical properties. The occupancies and local coordination environments of $Ln^{3+}$, $Cr^{3+}$, and $Te^{6+}$ cations will be characterized to evaluate any structural distortions.

## Experimental Methods

### Synthesis of $LnCrTeO_6$ (Ln= La, Pr, Nd)

To remove residual moisture, $La_2O_3$ (99.9%, TCI America), $Pr_2O_3$ (99.9%, Alfa Aesar), and $Nd_2O_3$ (99.997%, Alfa Aesar) powders were heated, in air to 900 °C and held for 12 hours. $Cr_2O_3$ (99.6%, Alfa Aesar) and $\alpha$-$TeO_2$ (99.99%, Alfa Aesar) were used as received. $Ln_2O_3$ (Ln= La, Pr, Nd), $Cr_2O_3$, and $\alpha$-$TeO_2$ were combined in a 1:1:2 molar ratios and thoroughly ground. Each sample was placed in separate alumina crucibles then put into a muffle furnace. Samples were heated in air at a rate of ~108 °C /h to 1000 °C for 10 hours and cooled to room temperature at a rate of ~108 °C /h. Samples were reground and reheated three times.

## Characterization Methods

### Powder X-ray Diffraction (PXRD)

Sample composition and purity was investigated using PXRD on a PANalytical Empyrean series 2 diffractometer with $\lambda$= 1.54056 Å, Cu-K$\alpha$ radiation, 45 kV, and 40 mA. The reflection-transmission-spinner stage was used with Bragg-Brentano model incident beam. XRD patterns were recorded at room temperature for the 2$\theta$ range 10-95° at a scan speed of 0.00889°/s with a step width of 0.004°. X'Pert Plus software package was used to analyze diffraction patterns and an established structural model was used for Rietveld refinement. The background was manually determined before preforming refinements and peak shape modeled with the pseudo-Voigt function. All samples contained two phases and both phase models were used simultaneously to first model the scale factor for each phase, then peak shape function using the Caglioto equation (U, V, W). Unit cell parameters, site occupancy, and isotropic displacement were refined. Global parameters that were refined were specimen displacement and zero shift.

### Diffuse reflectance spectroscopy (DRS)

DRS data was collected on a PerkinElmer Lambda 365 spectrophotometer accessorized with an integrating sphere from 200 to 1100 nm. Reflectance data was treated using the Kubelka-Munk function. This then allows for an estimation of direct and indirect bandgaps from Tauc plots.

## Background of methods used

### X-ray diffraction and the Rietveld method

X-ray diffraction (XRD) is used to determine the crystal structure of crystalline or semi-crystalline materials. X-rays are produced and projected toward the sample where constructive and destructive interferences occur between x-rays and the sample. The constructive interference is seen when Bragg's Law, $\lambda = 2d \sin\theta$, is satisfied. The separation between planes in the materials unit cell is denoted as d while $\theta$ values are chosen by the instrument user and $\lambda$ is a known value dependent upon the instrument's radiation source. The seven different crystal systems will produce peaks at different values of $2\theta$ unique to the type of crystal. The peak intensities are determined by the atoms (type and frequency of occurrence) in the unit cell and their positions on atomic planes. It is possible to manually calculate (hkl) planes that would occur given a specific crystal system and further find the identity of the material, but with the advancement of technology, matching patterns to previously reported data contained in a database is the norm. The user can use a calculated pattern and the Rietveld method to establish a model that fits well with the experimental data. Briefly, the Rietveld method uses the least squares method, a standard type of regression analysis, to model the experimental data and gives

the user measurements that allow quantification of the quality of the match between modeled and experimental data.[15]

## Kubelka-Munk theory and Tauc plots

Kubelka-Munk (K-M) theory relates the interaction between light and sample. The theory assumes that the sample is of finite thickness and infinite width and length, perfect diffusion and homogeneous illumination of the sample occurs, only scattering and absorption interactions occur between sample and light, the sample is isotropic and homogeneous, there is no external surface reflections, and that S and K are constant despite thickness.

$$F(R) = \frac{K}{S} = \frac{(1-R)^2}{2R} \quad (1)$$

Equation 1, often referred to as the Kubelka- Monk function, is the case when S > 0, K > 0, and L is infinity (thickness). Here, K represents the absorption coefficients and S is the scattering coefficients and both variables possess units of inverse length, making $F(R)$ dimensionless. Previous work has concluded that K and S depend on the intrinsic absorption and scattering coefficients, $\alpha$ and s respectively. Scattering phenomenon is neglected here so, s and S are considered constants. Equation 2 is used to construct a Tauc plot to approximate the band gap, denoted as $E_g$. Here, $h$ is Planck's constant, $\nu$ is equal to photon energy, $\gamma$ equals ½ for direct band gap and 2 for indirect band gap, and A is a proportionality constant. For simplicity, $F(R)$ is often denoted as α in Tauc plots and is such in Figures 9-11. The band gap is found from an extrapolation to zero, hence the y-axis of $(\alpha \times h\nu)^{1/\gamma}$ and x-axis of $h\nu$.[16]

$$(F(R_\infty) \times h\nu)^{1/\gamma} = A(h\nu - E_g) \quad (2)$$

## Results and Discussion

### Crystal Structure of $LnCrTeO_6$ (Ln = La, Pr, Nd)

Rietveld refinement of PXRD data collected on $LnCrTeO_6$ (Ln= La, Pr, Nd) show that all three samples crystallize with the $PbSb_2O_6$ structure type, in agreement with previous structural reports.[2-6] $LnCrO_3$ (Ln= La, Pr, Nd) was identified as a minority second phase. Rietveld refinements were performed for all three analogs to obtain unit cell dimensions and other details contained in tables 1-3. Unit cell volumes decrease as the atomic number of the Ln increases as expected due to the lanthanide contraction. A peak at $2\theta \sim 21°$ for each sample was indexed as the (101) reflection (Figures 2- 4). When the data is normalized, the (101) superstructure peak has a relative intensity of 0.0076(3), 0.0038(5), and 0.00382(2) for the La, Pr, and Nd analogs respectively; showing a decrease in intensity as Ln radius decreases, in agreement with previous work.[2-6] The changing intensities of the (101) peak in each analog suggests the possibility of a change in atom position, or the number of atoms present on that plane. From Rietveld refinements, it was found that Te occupancy varies between analogs and an occupancy of one for Te produces a very poorly fit model. Two peaks that can also be seen in Figures 2-4 insert, the (002) and (100) peaks, change in relative intensity with the different Te occupancies detailed in Tables 1 and 2. Figure 5 shows the hues of the three analogs where the La and Pr analogs are almost identical and the Nd analog seems to lose some of the green color and appears to contain more blue hues compared to the previous two.

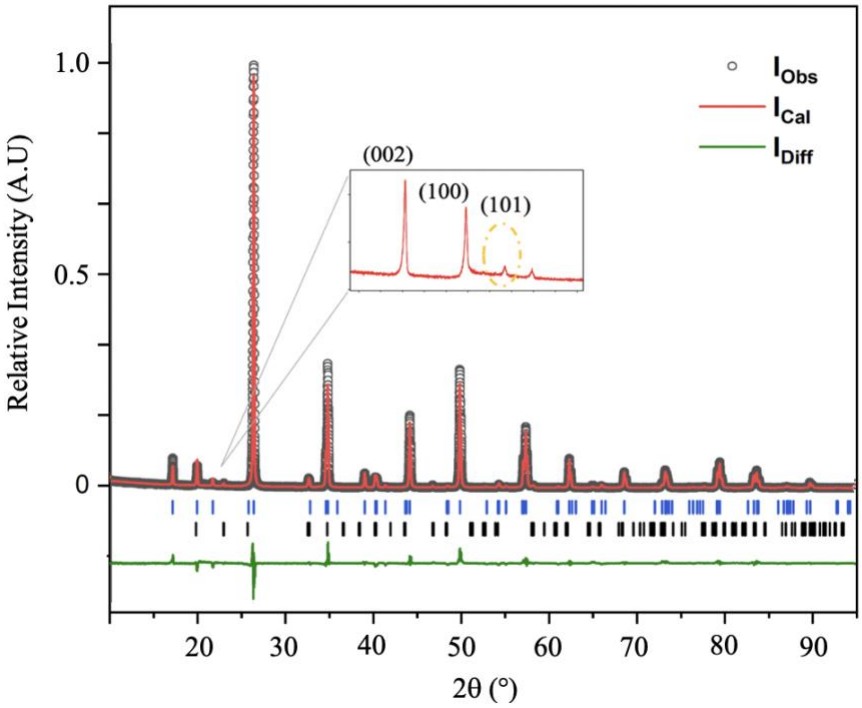


Figure 2: $LaCrTeO_6$ XRD refinement data showing the experimental and modeled data with blue tick marks indicating the main phase and black tick marks indicating the second phase $LaCrO_3$. Inset on graph shows the super structure peak located at 2θ ~ 21.7 °, circled in yellow.

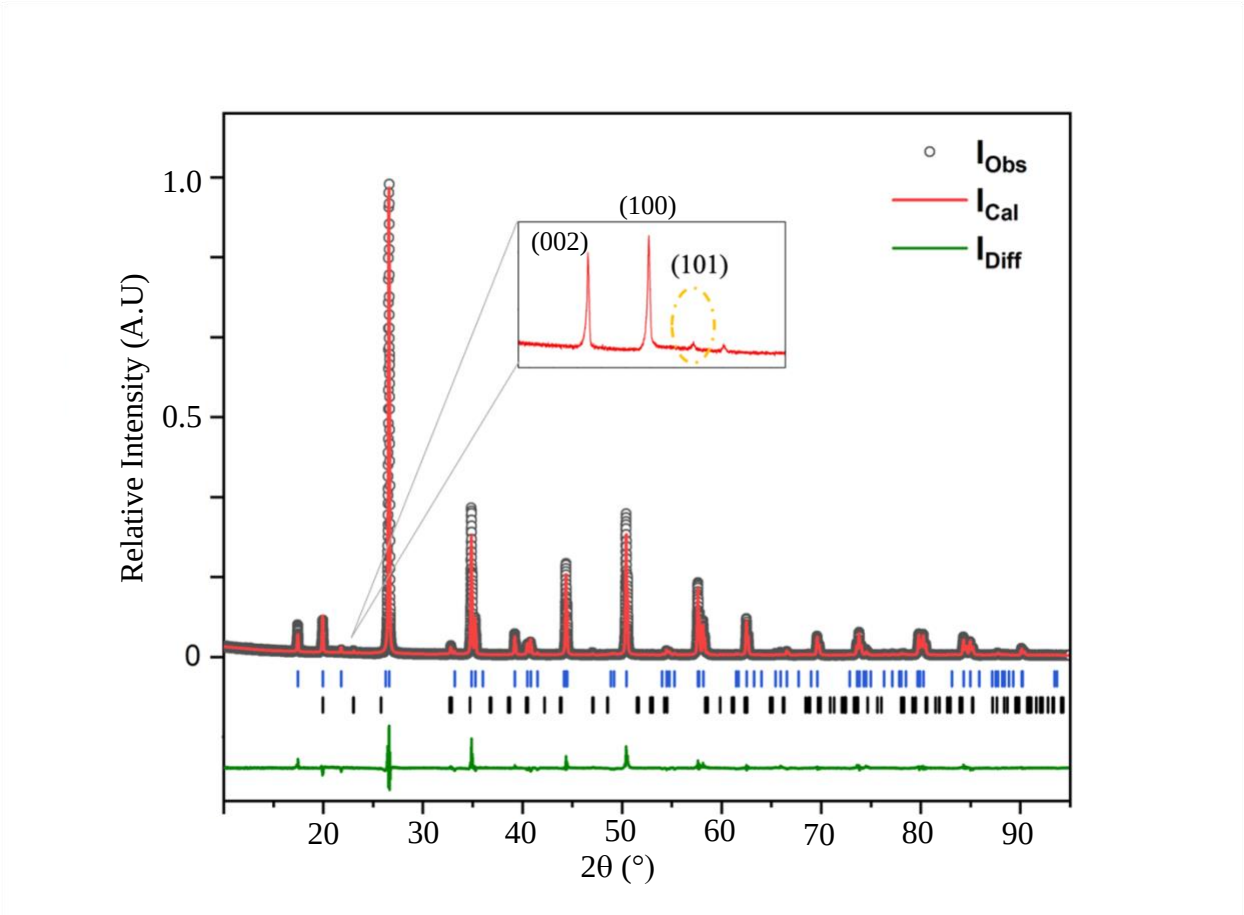


Figure 3: $PrCrTeO_6$ XRD refinement data showing the experimental and modeled data with blue tick marks indicating the main phase and black tick marks indicating the second phase $PrCrO_3$. Inset on graph shows the super structure peak located at 2θ ~ 21.8 °, circled in yellow.

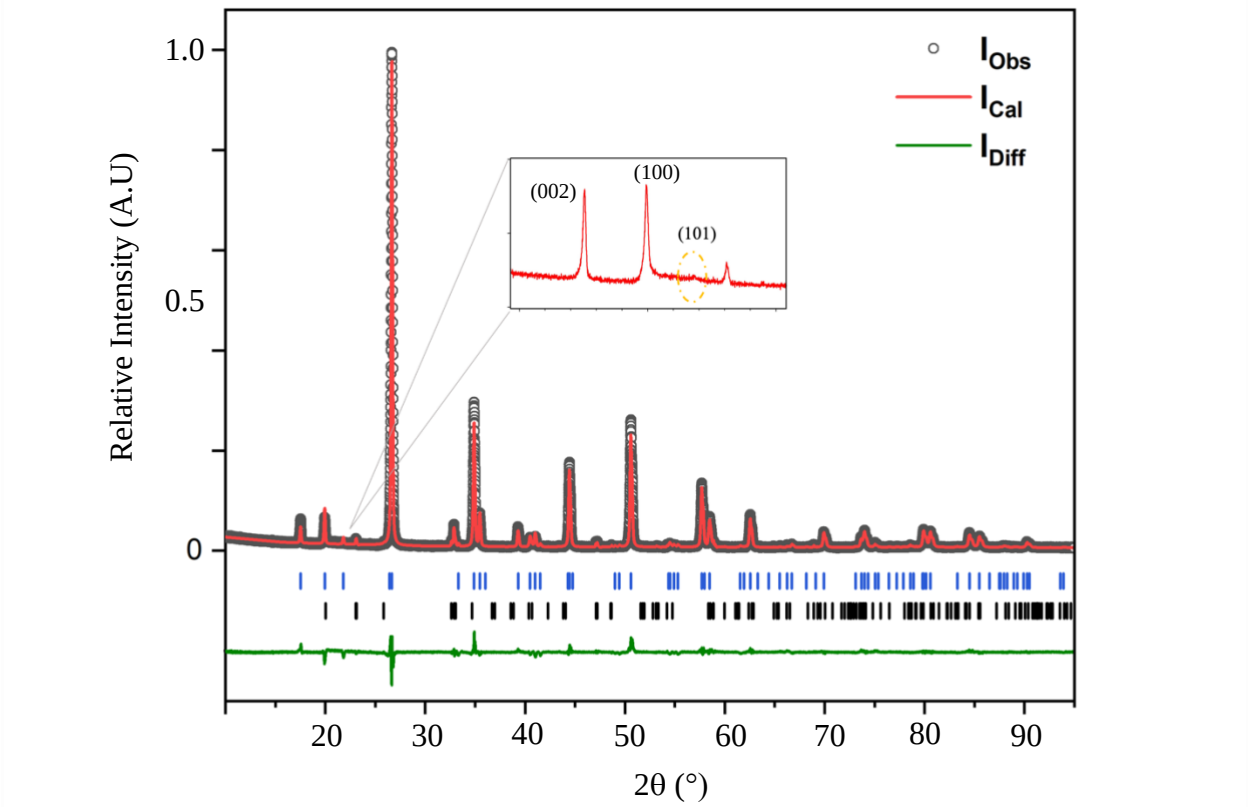


Figure 4: $NdCrTeO_6$ XRD refinement data showing the experimental and modeled data with blue tick marks indicating the main phase and black tick marks indicating the second phase $NdCrO_3$. Inset on graph shows the super structure peak located at 2θ ~ 21.8 °, circled in yellow.

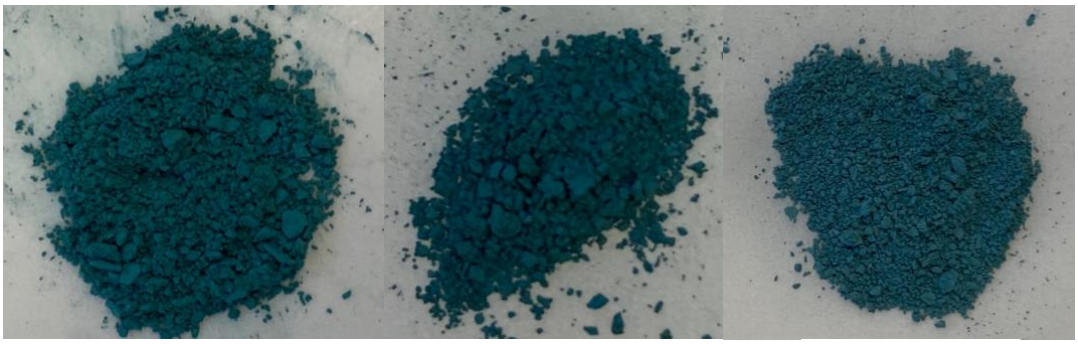

$LaCrTeO_6$ $PrCrTeO_6$ $NdCrTeO_6$

Figure 5: Photographs of $LnCrTeO_6$ (La, Pr, Nd)

Table 1: $LaCrTeO_6$ atomic positions and isotropic displacement parameters

| $R_{wp}$= 13.1014(4)%<br>GOF= 2.4307(2) | | **$LaCrTeO_6$** | **$LaCrO_3$** | | | |
|---|---|---|---|---|---|---|
| Crystal system | | Trigonal (Hexagonal axes) | Orthorhombic | | | |
| Space group (No.) | | $P\bar{3}$(147) | *Pnma* (62) | | | |
| Unit cell dimensions | | *a* = 5.1572(1) Å | *a* = 5.4806(6) Å | | | |
| | | *b* = 5.1572(1) Å | *b* = 7.7571(2) Å | | | |
| | | *c* = 10.3742(3) Å | *c* = 5.5134(7) Å | | | |
| | | α = β = 90°, γ = 120° | α = β = γ = 90° | | | |
| Volume | | 238.956(5) $Å^3$ | 234.400(3) $Å^3$ | | | |
| | Atom label | Wycoff site | x | y | z | occupancy | $B_{iso}$ ($Å^2$) |
| **$LaCrTeO_6$** | La(1) | 1*a* | 0 | 0 | 0 | 1 | 0.7083(7) |
| | La(2) | 1*b* | 0 | 0 | 1/2 | 1 | 0.6889(1) |
| | Cr(1) | 2*d* | 1/3 | 2/3 | 0.2497(2) | 1 | 0.5 |
| | Te(1) | 2*d* | 1/3 | 2/3 | 0.7499(2) | 0. 6833(2) | 0.313(7) |
| | O(1) | 6*g* | 0.0062(8) | 0.3673(3) | 0.1616(6) | 1 | 0.3991(5) |
| | O(2) | 6*g* | 0.3554(4) | 0.3780(8) | 0.3384(8) | 1 | 0.8749(3) |
| **$LaCrO_3$** | La(1) | 4*c* | -0.0022(8) | 0.25 | -0.0022(8) | 0.9927(9) | 0.4276(7) |
| | Cr(1) | 4*b* | 0 | 0 | 0.5 | 1 | 0.495(1) |
| | O(1) | 4*c* | 0.4267(4) | 0.25 | -0.0176 (6) | 0.9755(0) | 0.3421(2) |
| | O(2) | 8*d* | 1.8090(5) | 1.1416(6) | 0.1956(2) | 0.9867(1) | 0.4016(3) |

Table 2: $PrCrTeO_6$ atomic positions and isotropic displacement parameters

| $R_{wp}$= 11.9691(2)%<br>GOF= 2.2581(7) | | | **$PrCrTeO_6$** | | **$PrCrO_3$** | | |
|---|---|---|---|---|---|---|---|
| Crystal system | | | Trigonal | | Orthorhombic | | |
| Space group (No.) | | | $P\bar{3}$ (147) | | *Pnma* (62) | | |
| Unit cell dimensions | | | *a* = 5.1447(2) Å<br>*b* = 5.1447(2) Å<br>*c* = 10.1811(8) Å<br>α = β = 90°, γ = 120° | | *a* = 5.4791(5) Å<br>*b* = 7.7162(8) Å<br>*c* = 5.4490(3) Å<br>α = β = γ = 90° | | |
| Volume | | | 233.373(5) Å$^3$ | | 230.377(8) Å$^3$ | | |
| | Atom label | Wycoff site | *x* | *y* | *z* | occupancy | $B_{iso}$ (Å$^2$) |
| **$PrCrTeO_6$** | Pr(1) | 1*a* | 0 | 0 | 0 | 0.9810(1) | 0.5781(7) |
| | Pr(2) | 1*b* | 0 | 0 | 1/2 | 0.9903(3) | 0.5553(1) |
| | Cr(1) | 2*d* | 1/3 | 2/3 | 0.2498(6) | 1 | 0.5 |
| | Te(1) | 2*d* | 1/3 | 2/3 | 0.7497(4) | 0.6516(5) | 0.1419(4) |
| | O(1) | 6*g* | 0.0093(1) | 0.3650(5) | 0.1609(4) | 1 | 0.7980(2) |
| | O(2) | 6*g* | 0.3485(5) | 0.3678(7) | 0.3399(9) | 1 | 0.8853(7) |
| **$PrCrO_3$** | Pr(1) | 4*c* | 0.4605(6) | 0.25 | 0.0126(2) | 0.9965(4) | 0.3505(6) |
| | Cr(1) | 4*a* | 0 | 0 | 0 | 0.9928(8) | 0.2598(1) |
| | O(1) | 4*c* | 0.3933(7) | 0.0.25 | 0.6314(3) | 1 | 0.5 |
| | O(2) | 8*d* | 0.0924(3) | -0.0249(8) | 0.3348 (2) | 0.9094(2) | 0.4005(4) |

Table 3: $NdCrTeO_6$ atomic positions and isotropic displacement parameters

| $R_{wp}$= 9.8417(3)%<br>GOF= 1.9937(4) | | | **$NdCrTeO_6$** | | **$NdCrO_3$** | | |
|---|---|---|---|---|---|---|---|
| Crystal system | | | Trigonal | | Orthorhombic | | |
| Space group (No.) | | | $P\bar{3}$ (147) | | *Pnma* (62) | | |
| Unit cell dimensions | | | *a* = 5.1397(4) Å<br>*b* = 5.1397(4) Å<br>*c* = 10.1184(5) Å<br>α = β = 90°, γ = 120° | | *a* = 5.4872(3) Å<br>*b* = 7.6934(2) Å<br>*c* = 5.4203(8) Å<br>α = β = γ = 90° | | |
| Volume | | | 231.487(4) Å$^3$ | | 228.824(2) Å$^3$ | | |
| | Atom label | Wycoff site | *x* | *y* | *z* | occupancy | $B_{iso}$ (Å$^2$) |
| **$NdCrTeO_6$** | Nd(1) | 1*a* | 0 | 0 | 0 | 1 | 0.8105(2) |
| | Nd(2) | 1*b* | 0 | 0 | 1/2 | 1 | 0.8016(6) |
| | Cr(1) | 2*d* | 1/3 | 2/3 | 0.2487(2) | 1 | 0.5 |
| | Te(1) | 2*d* | 1/3 | 2/3 | 0.7499(1) | 0.689(5) | 0.1594(7) |
| | O(1) | 6*g* | -0.0029(1) | 0.3576(6) | 0.1494(5) | 1 | 0.5 |
| | O(2) | 6*g* | 0.3469(9) | 0.3988(4) | 0.3322(6) | 1 | 0.8172(3) |
| **$NdCrO_3$** | Nd(1) | 4*c* | 0.4658(2) | 0.25 | 0.0073(1) | 0.9965(4) | 0.4652(9) |
| | Cr(1) | 4*a* | 0 | 0 | 0 | 0.9928(8) | 0.0140(6) |
| | O(1) | 4*c* | 0.3713(1) | 0.0.25 | 0.5061(6) | 1 | 0.0556(2) |
| | O(2) | 8*d* | 0.1551(5) | -0.0215(1) | 0.3348 (2) | 0.9094(2) | 0.9417(1) |

## Distortions in LnCrTeO6 (Ln = La, Pr, Nd) octahedra

Experimental bond distances and bond angles for $LnCrTeO_6$ (Ln = La, Pr, Nd) are provided in Tables 4 and 5. For each analog, the Ln-O bond lengths consist of the two Ln sites and the two Ln site octahedra have different bond lengths compared to one another but the bond lengths within a Ln1 or Ln2 octahedra are the same for all six bonds. Similarly, the two Te-O bond lengths in each analog are in proximity of one another and agree with calculated lengths. The Cr-O bond lengths are noticeably smaller than the expected values for a Cr(III) cation with octahedral coordination. Based on the summation of ionic radii, the Cr (III) – O and Cr (IV) – O bond lengths are expected to be ~ 2.015 and 1.95 Å, respectively.[19] These values agree with *d*(Cr – O) = 1.99 – 2.07 Å in $Cr_2O_3$[20] and *d*(Cr – O) = 1.80 and 1.95 Å[21] in $La_2ZnGeO_4:Cr^{4+}$ and $CrO_2$[20], respectively. The experimentally observed *d*(Cr – O) of ~ 1.6 – 1.9 Å suggest a Cr(IV) oxidation state. In the La and Pr analogs, the Cr1-O1 interatomic distance of 1.802/1.849 Å is nearly identical to the Cr1-O2 distance of 1.860/1.825 Å. In $NdCrTeO_6$ Cr-O1 distance is significantly greater than the Cr-O2 distance. $LnO_6$, $CrO_6$, $TeO_6$ octahedra deviate from the theoretical bond angle for an octahedra of 90° (Table 5). The extent of the octahedra distortions can be seen in Figures 6 and 7. Inspecting the $LnO_6$ (Ln= La, Pr, Nd) octahedral bond angles compared to the $(Te/Cr)O_6$ octahedra show significant differences. One could see this visually where the Te and Cr octahdra are noticeably distorted in each analog. Considering that the Cr and Te octahedra share an edge with one another these results are not surprising since the distortion of one will affect the other much greater than in the case of corner sharing as with $LnO_6$ and $(Te/Cr)O_6$ octahedra.

Table 4: Selected bond lengths of $LnCrTeO_6$ (La, Pr, Nd)

| Atom Pair | Experimental Distance (Å) | Theoretical Distance (Å) |
|---|---|---|
| | $LaCrTeO_6$ | |
| La1 – O1 (x6) | 2.518 | 2.432 |
| La2 – O2 (x6) | 2.528 | 2.432 |
| Cr1 – O1 (x6) | 1.802 | $3^+$: 2.015, $4^+$: 1.95 |
| Cr1 – O2 (x6) | 1.860 | $3^+$: 2.015, $4^+$: 1.95 |
| Te1 – O1 (x6) | 1.906 | 1.960 |
| Te1 – O2 (x6) | 1.960 | 1.960 |
| | $PrCrTeO_6$ | |
| Pr1 – O1 (x6) | 2.475 | 2.390 |
| Pr2 – O2 (x6) | 2.461 | 2.390 |
| Cr1 – O1 (x3) | 1.849 | $3^+$: 2.015, $4^+$: 1.95 |
| Cr1 – O2 (x3) | 1.825 | $3^+$: 2.015, $4^+$: 1.95 |
| Te1 – O1(x3) | 1.917 | 1.960 |
| Te1 – O2 (x3) | 1.958 | 1.960 |
| | $NdCrTeO_6$ | |
| Nd1 – O1 (x6) | 2.386 | 2.383 |
| Nd2 – O2 (x6) | 2.557 | 2.383 |
| Cr1 – O1 (x3) | 1.943 | $3^+$: 2.015, $4^+$: 1.95 |
| Cr1 – O2 (x3) | 1.673 | $3^+$: 2.015, $4^+$: 1.95 |
| Te1 – O1 (x3) | 1.930 | 1.960 |
| Te1 – O2 (x3) | 1.997 | 1.960 |

Table 5: Selected bond angles for $LnCrTeO_6$ (Ln= La, Pr, Nd)

| Bond Angle | (°) |
|---|---|
| $LaCrTeO_6$ | |
| O1 – La1 – O1 | 80.483 |
| O1 – La1- O1 | 99.517 |
| O2 – La2 – O2 | 80.876 |
| O2 – La2 – O2 | 99.124 |
| O1 – Cr – O1 | 97.937 |
| O1 – Cr – O2 | 88.341 |
| O1 – Cr – O2 | 77.862 |
| O2 – Cr – O2 | 96.210 |
| O1 – Te – O1 | 98.774 |
| O1 – Te – O2 | 73.051 |
| O1 – Te – O2 | 89.068 |
| O2 – Te – O2 | 99.880 |
| $PrCrTeO_6$ | |
| O1 – Pr1 – O1 | 80.935 |
| O1 – Pr1 – O1 | 99.065 |
| O2 – Pr2 – O2 | 80.957 |
| O2 – Pr2– O2 | 99.043 |
| O1 – Cr – O1 | 98.078 |
| O1 – Cr – O2 | 78.633 |
| O1 – Cr -O2 | 86.544 |
| O2 – Cr – O2 | 96.942 |
| O1 – Te – O1 | 99.338 |
| O1 – Te – O2 | 73.853 |
| O1 – Te – O2 | 87.350 |
| O2 – Te – O2 | 99.998 |
| $NdCrTeO_6$ | |
| O1 – Nd1 – O1 | 95.877 |

| | |
|---|---|
| O1 – Nd1 – O1 | 84.123 |
| O2 – Nd2 – O2 | 80.738 |
| O2 – Nd2 – O2 | 99.262 |
| O1 – Cr – O1 | 95.681 |
| O1 – Cr – O2 | 79.680 |
| O1 – Cr – O2 | 88.164 |
| O2 – Cr – O2 | 96.718 |
| O1 – Te – O1 | 94.719 |
| O1 – Te – O2 | 72.610 |
| O1 – Te – O2 | 89.050 |
| O2- Te - O2 | 103.884 |

From Figure 7, we can see that the Te (blue atom) octahedra of both $LaCrTeO_6$ and $PrCrTeO_6$ have two shown bond angles around 99 ° and 73 °. When comparing to the Nd analog, there seems to be a larger difference of its bond angles compared to the La and Pr analog. One angle in $NdCrTeO_6$ being ~103 ° which is much different compared to the small difference of ~0.1 ° between La and Pr analog bond angles. The Cr-O bond lengths of the Nd analog also significantly differ from the La and Pr analogs. La and Pr analogs have Cr-O bond lengths of ~1.8 Å while the two Cr-O bond lengths are 1.943 Å and 1.673 Å which are the largest and smallest Cr-O bond lengths seen among all analogs. The difference of the La and Pr analogs versus the Nd analog align with the color similarities mentioned earlier, where La and Pr are like each other, and Nd seems to be the outlier. It would be beneficial to repeat the synthesis of the three analogs to see if Nd still shows these differing qualities. Synthesis using other lanthanides may also shed some light on the difference of analogs and the changing hues depending on the chosen Ln.

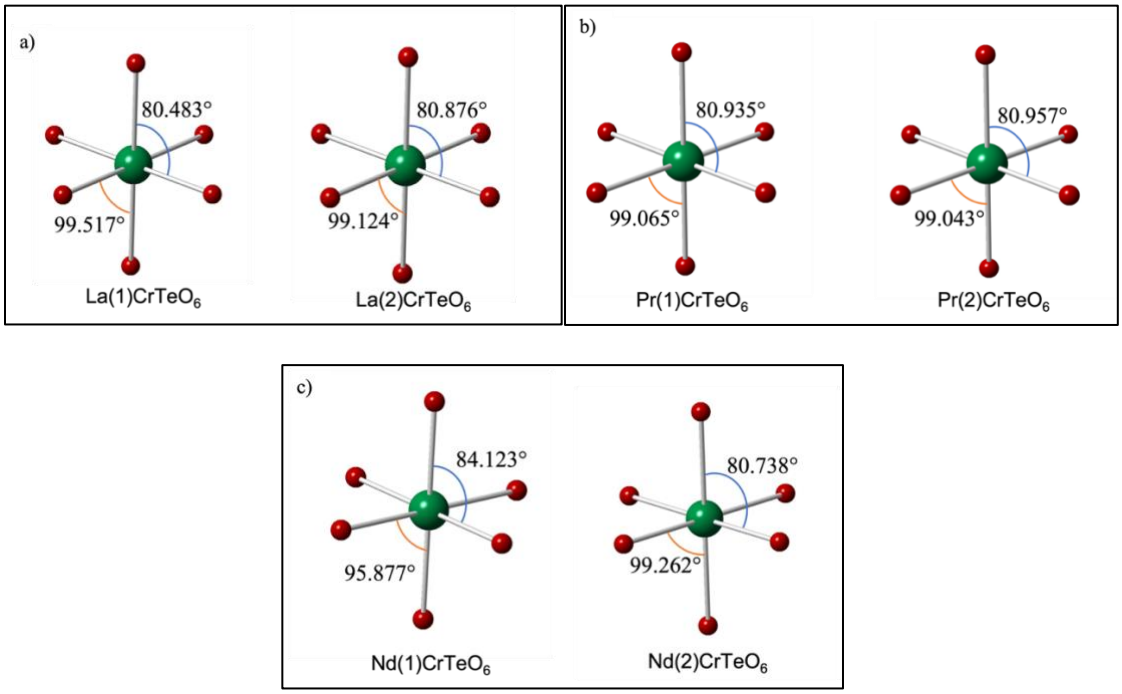


Figure 6: Bond angles of $LnO_6$ (Ln= La, Pr, Nd) octahedra.

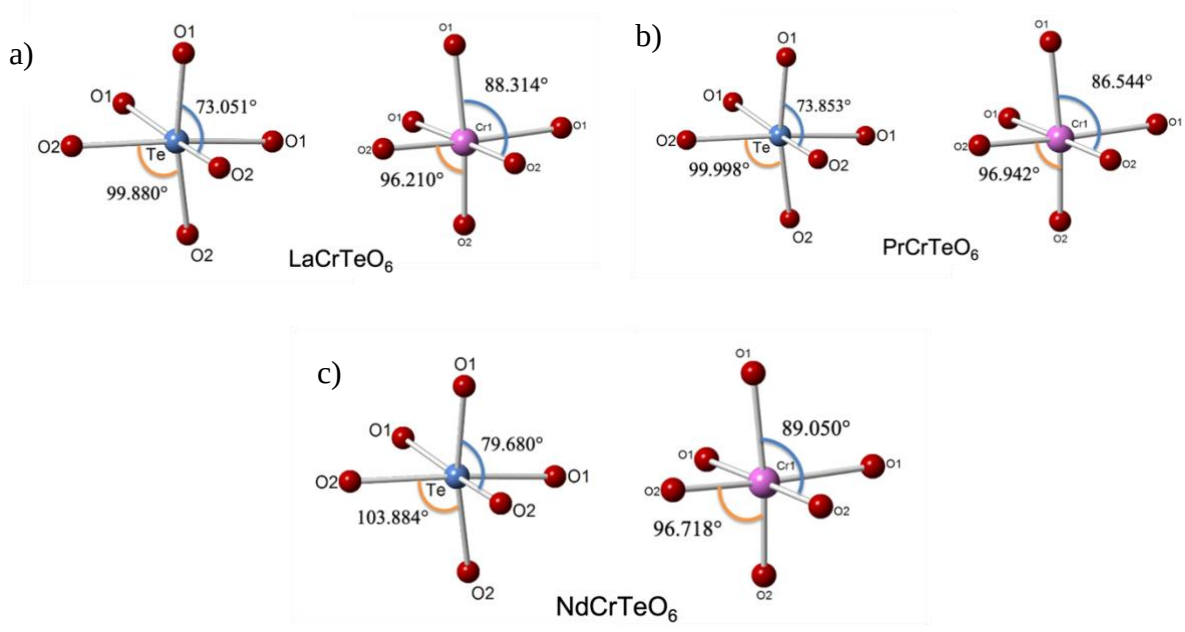


Figure 7: $TeO_6$ (blue) and $CrO_6$ octahedra (pink) for a) $LaCrTeO_6$, b) $PrCrTeO_6$, and c) $NdCrTeO_6$

## Optical Characterization

Diffuse reflectance spectroscopy (DRS) data is depicted in Figure 8, showing all samples following the same general curve. Reflectance is a quantitative measure of the wavelength of incident radiation an object does not absorb. Consequently, in the visible range of the electromagnetic spectrum, the reflectance represents the perceived color of an object. The peak with an onset of ~350 nm is most likely due to known impurities present in the sample, $LaCrO_3$, previously reported to have a band gap between 3.5–4 eV, which corresponds to wavelengths of 310–354 nm.[18] In Pr and Nd samples, the $LnCrO_3$ (Pr, Nd) impurity is present and is isostructural with $LaCrO_3$, suggesting that the ~350 nm peak seen in Pr and Nd DRS curves may be attributed to $LnCrO_3$ (Pr, Nd). Using data from the ~500 nm peak, the Kubelka-Munk function was applied for the construction of a Tauc plot which was then used to estimate direct and indirect band gaps (Figures 9-11). The details of the K-M function and construction of the Tauc plot are seen in the background of methods section. Direct and indirect band gaps are very close to one another across the three samples. It should be noted that the accuracy of K-M function and Tauc plots are still highly debated, and the band gaps are a rough estimation. From the La to Nd analogs, the direct and indirect band gaps generally increase but the change is very subtle which aligns with the small visual changes in color seen in Figure 5. These band gaps are in the expected range of 2.5- 2.9 eV for a blue-green material.[22]

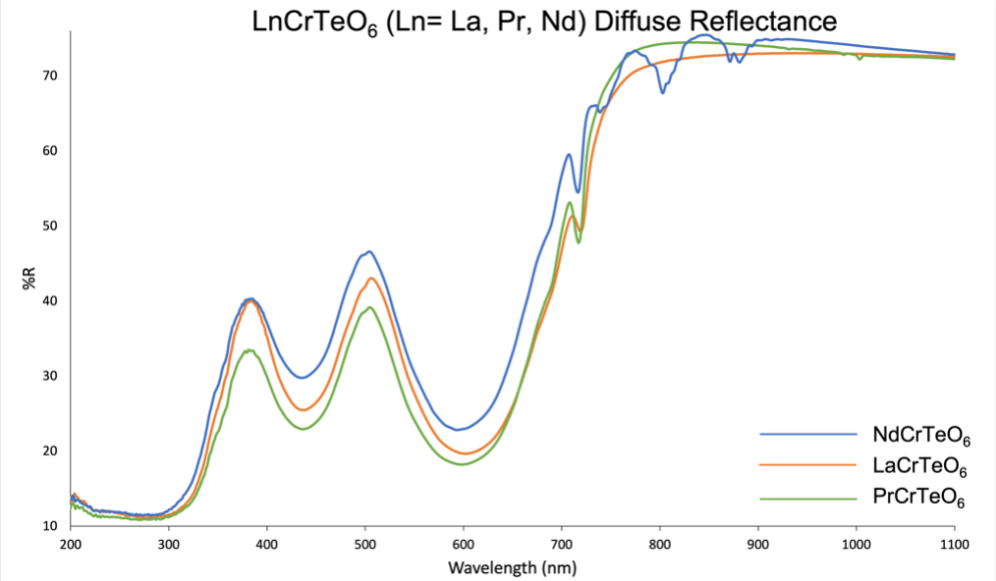


Figure 8: Diffuse reflectance spectra for $LnCrTeO_6$ (La, Pr, Nd)

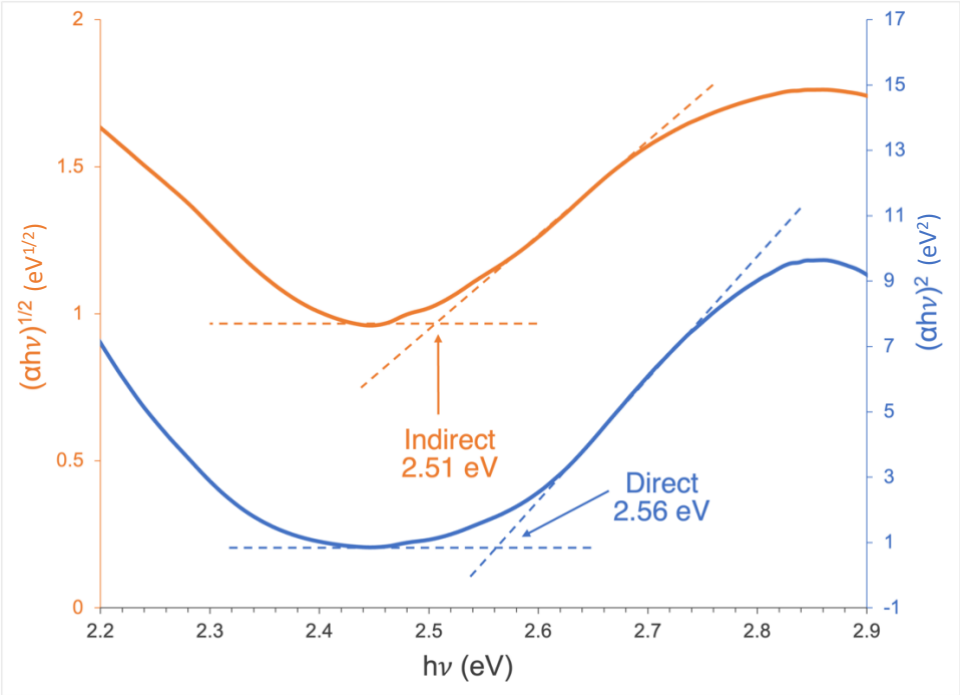


Figure 9: Direct and Indirect band gaps for $LaCrTeO_6$

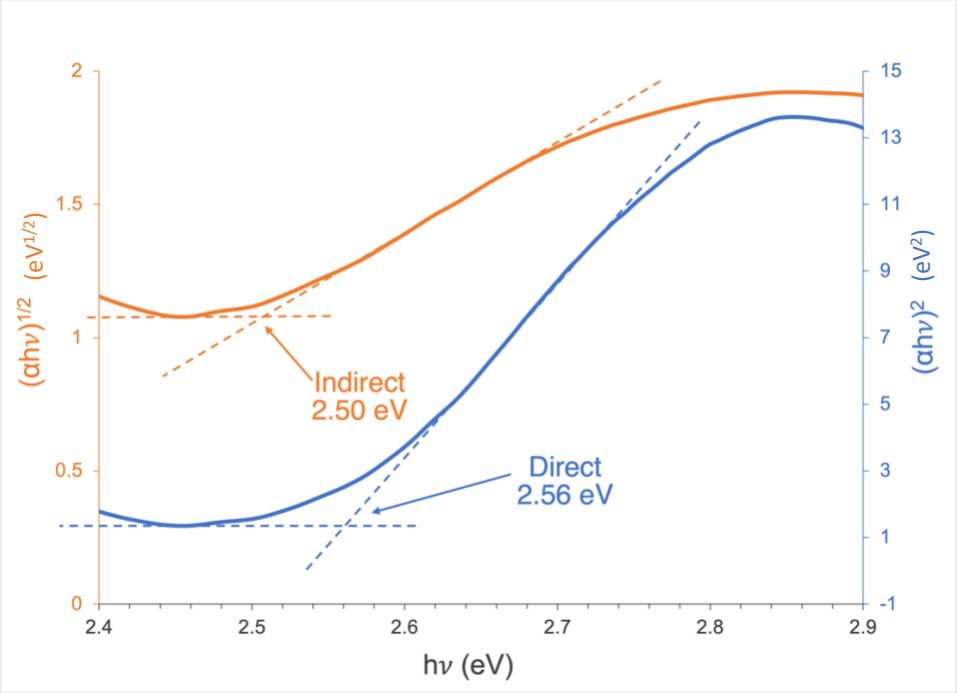


Figure 10: Direct and Indirect band gaps for $PrCrTeO_6$

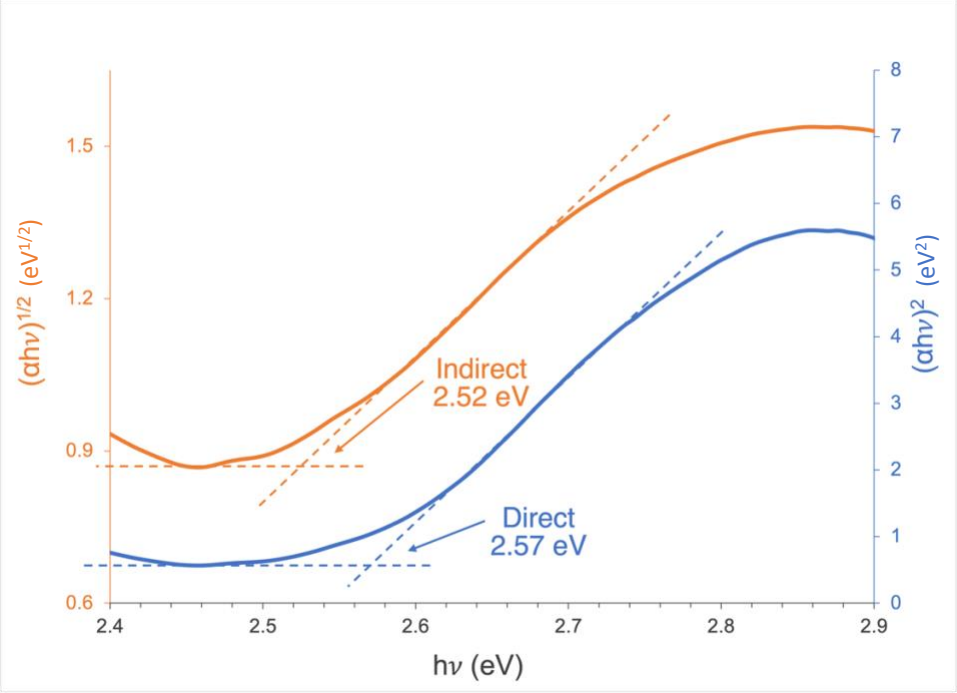


Figure 11: Direct and Indirect band gaps for $NdCrTeO_6$

## Conclusions and Outlook

In summary, LnCrTeO6 (La, Pr, Nd) compounds were synthesized using solid-state techniques and further characterized using optical methods and examination of coordination environments. The structural and optical characterization provides new insight of $LnCrTeO_6$ (La, Pr, Nd) distortions and optical properties. It is evident from the Ln (La, Pr, Nd), Cr and Te octahedral bond distances and angles that the octahedra in the compounds are distorted. The observed XRD patterns showing the (101) superstructure peak decrease in relative intensity form La to Nd analogs, correlating with the decrease in ionic radii and cell volume.

Modeling peak intensities of XRD patterns suggests the presence of Te deficiencies. Furthermore, Cr – O bond distances agree closely with Cr (IV) oxidation state. XRD experiments conducted for this thesis could not be used to detect oxygen deficiencies; therefore, complementary techniques such as neutron diffraction and electron dispersive spectroscopy (EDS) could be performed in the future. Optical properties examined with DRS allowed estimation of the direct and indirect band gaps of each sample. All band gaps were well within the expected range of 2.50- 2.57 eV for blue-green materials.

## References


1. A. Magnéll, The crystal structure of lead metaantimonate and isomorphous compounds. *Arkiv foer Kemi, Mineralogi och Geologi.* **1941**, 15, 1-6.

2. Basso, R.; Lucchetti, G.; Zefiro, L.; Palenzona, A. Rosiaite, $PbSb_2O_6$, a new mineral from the Cetine mine, Siena, Italy. *European Journal of Mineralogy* **1996,** 8 (3), 487-492.

3. Kasper, H. M.; Laboratory, L. $LnCrTeO_6$- A New Series of Compounds Based on the $PbSb_2O_6$ Structure. *Materials Research Bulletin* **1969,** *4* (1), 33-38.

4. Gayo, G. X.; Troncoso, F.; Lavat, A. E., Application of LnCrTeO6 Oxides as New Ceramic Pigments of the Type "Green Chromium." *Ceramics International* **2014**, *40* (1), 611–

5. Gupta, N. K.; Roy, S. P.; Joshi, P.V.; Ramma Rao, G. A.; Krishnan, K.; Singh Mudher, K. D., X-Ray and thermal investigations of $LaFeTeO_6$ and $LaCrTeO_6$ compounds. *Journal of Alloys and Compounds* **2006,** 417, 300-303.

6. Rao, G. N.; Sankar, R.; Panneer Muthuselvama, I.; Chou, F. C., Magnetic and thermal property studies of RCrTeO6 (R= trivalent lanthanides) with layered honeycomb sublattices. *Journal of Magnetism and Magnetic Materials* **(2014),** *370*, 13-17.

7. Blasse, G. and De Pauw, A. D. M., Compounds with lead antimonate structure. *Journal of Inorganic and Nuclear Chemistry* **1970,** 32, 2533-2537

8. Lavat, A. E.; Mercader, R. C.; Baran, E. J., Crystallographic and spectroscopic characterization of LnFeTeO6 (Ln = La, Pr, Nd, Sm) materials. *Journal of Alloys and Compounds* **2010,** *508*, 24-27.

9. Egorysheva, A.V.; Ellert, O.G.; Liberman, E.Y.; Kirdyankin, D.I.; Golodukhina, S.V.; Gajtko, O.M.; Svetogorov, R.D. Synthesis and characterization of new isostructural series $LnFe_{0.5}Sb_{1.5}O_6$ (Ln = La-Sm) exhibiting high catalytic activity in CO oxidation. *Journal of Alloys and Compounds* **2019,** 777, 655- 622.

10. Egorysheva, A.V.; Golodukhina, S.V.; Khoroshilov, A.V.; Tyurin, A.V.; Gajtko, O.M.; Svetogorov, R.D.; Trigub, T.L. Synthesis, structural feature and properties of rosiait structure compound $BiGeSbO_6$. *Ceramics International* **2020,** 46, 7413- 7420.

11. Spooner, K.B.; Ganose, A.M.; Winnie Leung, W.W.; Buckeridge, J.; Williamson, B.A.D.; Palgrave, R.G.; and Scanlon, D.O. $BaBi_2O_6$: A Promising n-Type Thermoelectric Oxide with $PbSb_2O_6$ Crystal Structure. *Chemistry of Materials* **2021,** 33, 7441-7456.

12. Hallas, A. M. and Morosan, E., $Sr(M, Te)_2O_6$ (M= Cr, Mn, Fe, Co, Ni): A Magnetically Dilute Family of Honeycomb Tellurates. *Inorganic Chemistry* **2019,** 58, 10, 6993-6999.

13. Kim, S. W.; Deng, Z.; Li, M.; Gupta, A. S.; Akamatsu, H.; Gopalan, V.; Greenblatt, M., A(II)$GeTeO_6$ (A = Mn, Cd, Pb): Non-Centrosymmetric Layered Tellurates with $PbSb_2O_6$-Related Structure. *Inorganic Chemistry* **2017,** 56, 9019- 9024.

14. Kim, S. W.; Deng, Z.; Fischer, Z.; Lapidus, S.H.; Stephens, P. W.; Li, M.; Greenblatt, M. Structure and Magnetic Behavior of Layered Honeycomb Tellurates, BiM(III)$TeO_6$ (M = Cr, Mn, Fe). *Inorganic Chemistry* **2016,** 55, 10229- 10237.

15. Cullity, B. D.; Stock, S. R. *Elements of X-ray Diffraction*, 3rd edition; Peason, 2001.

16. Choudhury, A. K. R. *Principals of Colour and Appearance Measurement*, Volume 2; Woodhead Publishing, 2015.

18. Arima, T.; Tokura, Y.; Torrance, J.B., Variation of optical gaps in perovskite-type Bd transition-metal oxides. *Physical Review B* **1993,** 48, 17006.

19. Atomic Simulation Group in the Materials Department of Imperial College. Database of Ionic Radii. http://abulafia.mt.ic.ac.uk/shannon/ptable.php? (accessed July 20 2022).

20. Jain, A.; Ong, S.P.; Hautier, G.; Chen, W.; Richards, W.D.; Dacek, S.; Choila, S.; Gunter, D.; Skinner, D.; Ceder, G.; and Persson, K. A., Commentary: The Materials Project: A materials genome approach to accelerating materials innovation. *APL Materials* **2013,** 1, 011002.

21. Zhou, H.; Cai, H.; Zhao, J.; Song, Z.; Liu, Q., Crystallographic control for $Cr^{4+}$ activators toward efficient NIR-II luminescence. *Inorganic Chemistry Frontiers* **2022,** 9, 1912-1919.

22. Chemistry LibreTexts. Semiconductors-Band Gaps, Colors, Conductivity, and Doping. https://chem.libretexts.org/Bookshelves/Inorganic_Chemistry/Book%3A_Introduction_to_Inorganic_Chemistry_(Wikibook)/10%3A_Electronic_Properties_of_Materials_-_Superconductors_and_Semiconductors/10.05%3A_Semiconductors-_Band_Gaps_Colors_Conductivity_and_Doping (accessed 1 August 2022).